



Contents lists available at ScienceDirect

Journal of Fluids and Structures

journal homepage: www.elsevier.com/locate/jfs



Gust load alleviation on an aircraft wing by trailing edge Circulation Control

Yonghong Li ^{a,b,1}, Ning Qin ^{a,*1}

^a Department of Mechanical Engineering, University of Sheffield, Sheffield, England S1 3JD, United Kingdom

^b High Speed Aerodynamics Institute, China Aerodynamic Research and Development Center, Mianyang, China



ARTICLE INFO

Article history:

Received 16 July 2020

Received in revised form 2 September 2021

Accepted 23 September 2021

Available online 6 October 2021

Keywords:

Gust load alleviation

Wing aerodynamic and structural

interaction

Circulation control

Elastic wing

ABSTRACT

This paper reports an investigation of gust load alleviation using Circulation Control for a three-dimensional wing including aerodynamic and structure interaction. The Field Velocity Method is introduced to the unsteady Reynolds averaged Navier-Stokes solutions for gust response simulations. Structural dynamic equations of motion are coupled with the unsteady Reynolds averaged Navier-Stokes solutions to consider the aeroelastic effects due to the gust response. The effects of gust load alleviation on the BAH wing using Circulation Control are tested under typical 'one-minus-cosine' gust profiles from certification specification defined by European Aviation Safety Agency. The results show a promising capability of Circulation Control for gust load alleviation as significant gust load alleviation effects have been achieved for both the rigid and elastic BAH wings in the test cases. For the BAH wing considering aeroelasticity, the displacement oscillations induced by gusts have been effectively suppressed by Circulation Control. The results also show that Circulation Control has the fast frequency response characteristics, where more than 50% of the total change in lift coefficient can be obtained within the non-dimensional time $s = \frac{U_{ext}}{\bar{c}} = 1$.

© 2021 Elsevier Ltd. All rights reserved.

1. Introduction

Gusts are of critical importance to aircraft designs, as gust loads often define the maximum loads that the aircraft structures will experience in flight. In the design process, there are a large number of gust load cases to be considered. It is expensive and time-consuming if experimental data are required for all design cases. Therefore, if gust load calculations can be made using Computational Fluid Dynamics (CFD) data in place of experimental data, they can be used earlier in the design process and reduce the need for wind tunnel tests. In recent years, a great effort has been given to the numerical simulations for gust response. A collaborative research project between industry and academia named AeroGust ([Bekemeyer et al., 2019](#)) (Aeroelastic Gust Modelling) is funded by the European Union's Horizon2020 Research and Innovation program, aiming to investigate and develop simulation methods for gusts and to investigate gust interactions with aircraft. For the well-known CFD software, elsA in ONERA ([Huvelin et al., 2019](#)), DLR-TAU ([Neumann and Mai, 2013](#)), FUN3D in NASA ([Bartels, 2012](#)) and EZNSS ([Levy, 2001](#)) (elastic zonal Navier-Stokes simulation) CFD codes have been enhanced and used for gust response simulations.

An important topic associated with gust is gust load control or gust load alleviation, because it can potentially provide a substitute approach to reduce drag by reducing the aircraft structure weight. Since the aircraft structure mass is

* Corresponding author.

E-mail address: n.qin@sheffield.ac.uk (N. Qin).

¹ The paper written by the two co-authors with equal contributions.

Nomenclature

A	Reference area [m^2]
C_L	Lift coefficient
C_p	Pressure coefficient
C_{mx}	Wing root bending moment coefficient
c_{ref}	Mean aerodynamic chord length [m]
$C_\mu = \frac{\dot{m}U_{jet}}{q_\infty A}$	Momentum coefficient
$C_{\mu 0}$	Peak momentum coefficient
H_g	Gust wavelength [m]
k	Reduced frequency
l	Wing span [m]
M	Mach number
\dot{m}	Mass flow rate [kg/s]
q_∞	Is the freestream dynamic pressure,
$Re_{c_{ref}}$	Reynolds number based on mean aerodynamic chord
$s = \frac{U_\infty t}{c}$	Non-dimensional time
U_∞	Freestream velocity [m/s]
U_{jet}	Jet velocity [m/s]
w_{g0}	Peak velocity of 'one-minus-cosine' gusts
x, y, z	Cartesian coordinates in streamwise, spanwise and vertical directions [m]
α	Angle of attack [deg]

determined by the critical extreme loads not the cruise state, which in most cases are gust loads (Guo et al., 2015), large amounts of structure mass penalty must be made to cope with gust loads. However, an aircraft commonly spends the most time in the cruise condition, not under the gust conditions. Therefore, if the short-period gust loads that an aircraft may experience in flight can be well controlled, lighter aircraft structure may be designed. As a consequence, a reduced lift is needed and this in turn reduces the lift-dependent drag.

Control flaps, such as spoilers, elevators and ailerons are normally used by current civil aircraft to control gust loads (Frederick et al., 2010; Ng et al., 2016). The first commercial airplane incorporating a Gust Load Alleviation (GLA) system using ailerons is the Tristar L-1011 from the 1980s (ohnston, 1979), and later both ailerons and spoilers were implemented in the GLA system on Airbus A320 (Payne, 1986). During the following decades, research in gust alleviation has been focused on the GLA system designs, especially in the field of design of control laws (Liu and Sun, 2017; Liu et al., 2018) using control surfaces (Szczyglowski et al., 2019) and wing-tip devices (Cheung et al., 2018). However, the aforementioned gust alleviation using control surfaces has a difficulty to achieve high-frequency response. As pointed out by Al-Battal et al. (2018), control surfaces are sized for maneuvers and therefore become ineffective at high gust frequency due to their large inertia.

Fluidic actuators offer the potential for fast control response time. They include blowing or suction, synthetic jets and circulation control using the Coanda effect. Being able to fly and control aircraft without conventional control surfaces (namely flapless control) is one of the targets for future aircraft design with fewer moving parts, therefore less weight (Paterson et al., 2004), less maintenance and enhanced stealth characteristics (Anonymous, 2006). Since fluidic actuators are capable for lift augmentation, they can equally reduce and manage lift, which provides the potential for gust load alleviation. To this end, some initial investigations on the potential application for reducing lift have been conducted recently. de Vries et al. (2009) carried out numerical researches on a normal jet blowing located near the NACA0018 aerofoil upper trailing edge surface at a freestream Mach number of 0.176, and showed a significant lift reduction. Al-Battal et al. (2018) experimentally compared the effects of normal jet blowing and counter blowing for lift reduction. The results indicated that both approaches are capable for lift reduction. Unlike the surface jet blowing working in the direction that is perpendicular to aircraft surfaces, circulation control (CC) by Coanda effect uses the tangential trailing-edge surface jet blowing. CC has attracted much attention for the researches on flight controls by using this method for altering the circulation around the aircraft wings in recent years (Hoholis et al., 2016). The Coanda effect describes the tendency of high-speed jet flow staying attached to the Coanda devices which commonly have convex surfaces, due to the combined effects between the centrifugal force and the low static pressures formed by the jet flow. The high-speed jet flow will entrain the external flow around the aerofoil or wing surface to follow the jet flow as to "bend down" over the curved Coanda surface when the jet slot is placed on the upper surface. This will accelerate the external flow and generate a net increase of the circulation, which results in the increased lift. Similarly, lift reduction can be obtained when placing the jet slot on the lower surface. A number of experiments and numerical studies have been conducted on CC effectiveness for lift augmentation or reduction (Cook et al., 2008; Alexander et al., 2005), on Coanda surface design (Forster and Steijl, 2017),

on aircraft flight control (Hoholis et al., 2016; Wilde et al., 2010), on turbine cascade performance improvement (Song et al., 2011) and on CFD validation (Min et al., 2009; Forster and Steijl, 2015; Rumsey and Nishino, 2011).

In a previous article by the authors (Li and Qin, 2019), the feasibility and effects of gust load alleviation by CC was firstly demonstrated on the two-dimensional (2D) NACA0012 aerofoil numerically. The results showed a promising gust load alleviation effect, especially under subsonic incoming flows. To gain insights into the influence of three-dimensional (3D) effects (e.g. the load control effects on the whole span if Coanda surface is only deployed on a segmental span) and the aeroelasticity on gust responses, this article will take a further step to conduct the investigation based on the BAH wing (Bisplinghoff et al., 1996). Validations for gust responses of rigid models have been presented in Li and Qin (2019). For the consideration of aeroelasticity in gust responses, structural dynamic equations of motion are coupled with the URANS solutions. This is validated through the gust responses of the elastic BAH wing to a square-wave gust in Section 3, following by a numerical model setup for BAH wing with Coanda surface around the wing-tip region. Load control capabilities and responses of dynamic actuation of CC are evaluated under steady subsonic and transonic incoming flows in Section 4. Thereafter, the effects of gust load alleviation of the BAH wing using CC are tested under typical ‘one-minus-cosine’ gusts from certification specification (CS-25) defined by European Aviation Safety Agency (EASA) (Anon, 0000) in Section 5.

2. Numerical methods

2.1. URANS solver

The numerical solver is the NASA Open CFD software CFL3D (Scalfani et al., 2014). It is a multi-block structured upwind finite volume CFD code. The 3-D time-dependent compressible Navier–Stokes equations can be expressed in an integral form as follows:

$$\frac{\partial}{\partial t} \iiint \mathbf{W} dV + \iint [\mathbf{F} - \mathbf{G}] \cdot d\mathbf{A} = 0 \quad (1)$$

where, t is the time, \mathbf{W} is the conserved variables; V is an arbitrary control volume; \mathbf{F} and \mathbf{G} are the inviscid and viscous fluxes, respectively; $d\mathbf{A}$ is the vector of the differential surface area.

The variables and the fluxes are

$$\mathbf{W} = \begin{bmatrix} \rho \\ \rho v_x \\ \rho v_y \\ \rho v_z \\ e \end{bmatrix}, F = \begin{bmatrix} \rho \mathbf{v} \\ \rho \mathbf{v} v_x + p \hat{\mathbf{i}} \\ \rho \mathbf{v} v_y + p \hat{\mathbf{j}} \\ \rho \mathbf{v} v_z + p \hat{\mathbf{k}} \\ (e + p) \mathbf{v} \end{bmatrix}, G = \begin{bmatrix} 0 \\ \tau_{xi} \\ \tau_{yi} \\ \tau_{zi} \\ \tau_{ij} v_j - \mathbf{q} \end{bmatrix}$$

where, ρ , p , e , and \mathbf{v} are the density, pressure of the fluid, total energy per unit volume, and velocity, respectively. τ_{ij} is shear stress, and \mathbf{q} is the heat flux.

For the convective terms, a 3rd order upwind-biased spatial differencing (Roe scheme) is used, and the viscous terms are discretized by second-order central differencing. For the turbulence model, $k-\omega$ SST model is used in this study.

CFL3D has the capability to perform both static and dynamic aeroelastic analysis. CFL3D performs aeroelastic analysis by solving the aeroelastic equations of motion in the generalized modal state space as:

$$\mathbf{M} \ddot{\mathbf{q}} + \mathbf{C} \dot{\mathbf{q}} + \mathbf{K} \mathbf{q} = \mathbf{Q}, \mathbf{q}^T = [q_1, q_2 \dots] \quad (2)$$

where \mathbf{q} is generalized displacement vector; \mathbf{K} is generalized stiffness matrix; \mathbf{C} is generalized damping matrix; \mathbf{M} is the generalized mass matrix, and \mathbf{Q} is generalized force.

The time matching of the fluid/structure coupling uses a second-order backward differencing and a predictor/corrector scheme, which can be found in Ref. Edwards et al. (1983) for more details. Since the fluid dynamics solver is also second order, therefore, the overall scheme is second order accurate. The mesh deformation uses the exponential decay method. Prior to running the CFL3D code for fluid-structural calculations, frequencies, generalized masses, and mode shapes should be provided and projected onto the grid points of the computational model surface.

2.2. Field velocity method

Parameswaran and Baeder (1997) and Singh and Baeder (1997) was the first to use URANS solutions to simulate the indicial responses of a 2D aerofoil to a step change in the angle of attack and gusts. The incorporated so-called ‘Grid Velocity Method’ or ‘Field Velocity Method’ (FVM) into a Euler/Navier–Stokes solver was used to introduce the gust perturbations into the flow domain by prescribing the gust velocity onto the velocities of the grid points. Arbitrary gust response simulations can be achieved by prescribing the velocities of the grid points varying based on the space and time. FVM is a significant advance in the field of gust response simulations and has been implemented into different CFD codes for gust load analyses, such as FUN3D (Bartels, 2012), EZNSS (Levy, 2001) (elastic zonal Navier–Stokes simulation) CFD

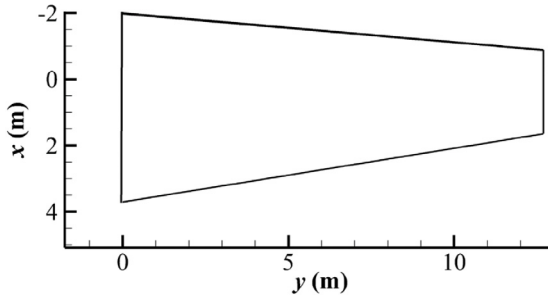


Fig. 1. Planform of the BAH wing.

code, *elsA* (Rigaldo and Borglund, 2011) and DLR-TAU Code (Timme et al., 2013). In the code programming, The prescribed gust velocity can be added to the mesh deformation velocity on every grid point depending on the space and time as:

$$v_{grid}[(x, y, z), t] \rightarrow v_{grid}[(x, y, z), t] - v_{gust}[(x, y, z), t] \quad (3)$$

Based on the dynamic mesh module in CFL3D, the functions based on FVM is added with the capability to simulate arbitrary gust shapes.

3. Validation and verification

3.1. Verification of trailing-edge circulation control

Verification of the solver and the boundary conditions for CC has been conducted and presented in Ref. Li and Qin (2019). The experimental data for the validation is from Alexander et al. (2005) for the test of CC effects on a semi-span wing with 0.75% cambered elliptic aerofoil having a thickness of 6% chord. The Coanda surface is 2.98:1 elliptical with a slot height to chord ratio of 0.12%. A good agreement between the present numerical results and the experimental data from subsonic to the transonic range had been obtained, which can be found in Ref. Li and Qin (2019).

3.2. Validation of gust simulation

FVM is introduced to the URANS solutions for the simulation of gust responses. The numerical responses of a series of gust profiles including a step-change in the angle of attack, sharp-edged gusts and the one-minus-cosine gusts using the 2D rigid NACA0012 aerofoil are compared to the Wagner function (Jones, 1940), Küssner function (Wright, 2015) and reference data from Ref. Raveh and Zaide (2006), respectively. Detailed results have been presented in Ref. Li and Qin (2019).

To consider the aeroelasticity and rigid motions due to the gust response, an additional validation work is done herein using the 3D BAH wing with the plunging and the first bending modes. The solver coupling URANS solutions, structural dynamic equations of motion and FVM are validated through the comparison between the present numerical results and the available data as demonstrated in the following section.

3.3. Gust response of the elastic BAH wing

The BAH wing is a jet transport wing, on which Bisplinghoff et al. (1996) conducted comprehensive investigations in the area of aeroelasticity. The BAH wing is a half wing with a wingspan $l = 12.7$ m, a mean aerodynamic chord $c_{ref} = 4.1275$ m, and a wing area $S = 52.42$ m². The BAH wing planform is shown in Fig. 1.

A wide range of aeroelastic test cases have been validated using the commercial software, MSC/NASTRAN (Corporation, 2002), with high-fidelity structural analysis (Howcroft et al., 2016). The BAH wing has been adapted by Rodden et al. (1979) as an MSC/NASTRAN demonstration problem in random gust response analysis. In MSC/NASTRAN, the aerodynamic force is introduced by Doublet Lattice Method (Albano and Rodden, 1969) ignoring the wing-section thickness effects. To compare with the MSC/NASTRAN data, the NACA65A004 aerofoil is used to construct the CFD model of the BAH wing. The mesh topology of the computational domain is shown in Fig. 2. The total grid size is about 4.0×10^6 .

The mode shapes are extracted from the structural model in MSC/NASTRAN and are projected to the grid points on the wing surface of the CFD model. In this study, two typical modes are included in the simulation. The first is the plunging mode with a natural frequency of 0 Hz and the second is the first bending elastic mode with a natural frequency of 2.44 Hz. The mode shape profiles are shown in Fig. 3.

In MSC/NASTRAN, the demonstration case calculates the time history of the displacement responses of the BAH wing due to a gust load. The gust is a square wave gust shown in Fig. 4 with a duration of 2 s. The freestream Mach number is 0.62 and the gust amplitude w_g is taken as 0.01 times the incoming flow velocity, which is 2 m/s.

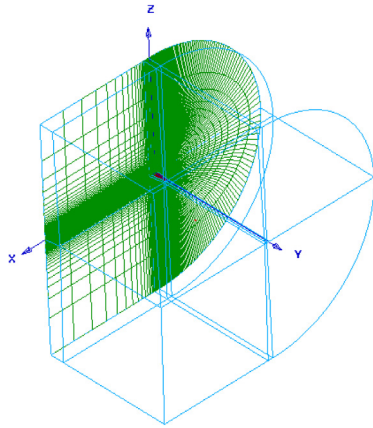
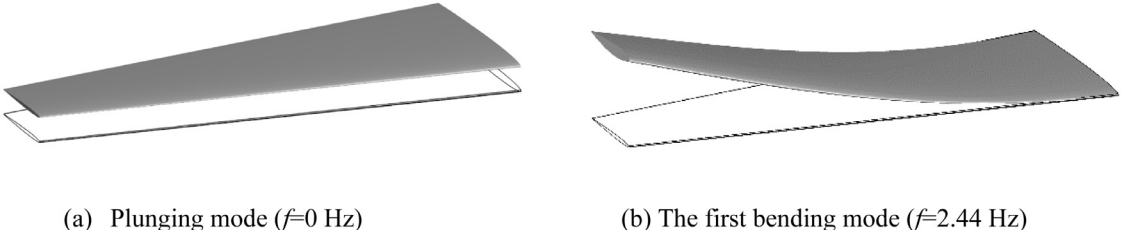


Fig. 2. Mesh topology of the BAH wing.



(a) Plunging mode ($f=0$ Hz) (b) The first bending mode ($f=2.44$ Hz)

Fig. 3. The mode shape profiles of the BAH wing.

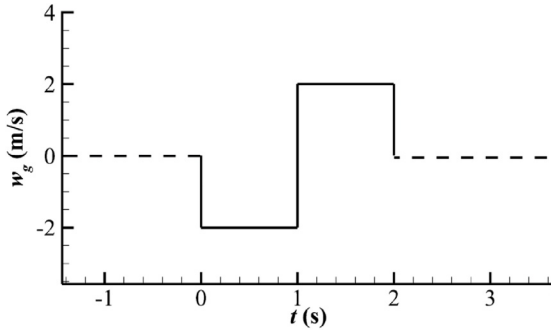


Fig. 4. The profile of the square wave gust.

The square wave gust is assigned to the grid points of the CFD domain based on the FVM. Based on the validation results in gust response simulations presented in Ref. Li and Qin (2019), the time step is taken as $\Delta s = 0.0125$. Fluid and structure are coupled in the present numerical solver as described in Section 2. Responses of the fluid–structure interactions of the BAH wing under this square wave gust is calculated by the present numerical solver. The vertical displacement responses are compared with the MSC/NASTRAN results (Corporation, 2002) shown in Fig. 5. The present results show a good agreement with that calculated by MSC/NASTRAN. This indicates that the present solver is capable of accurate gust response simulation of both rigid models and elastic models with motion.

4. Numerical model setup and load control evaluation

4.1. Numerical model setup of the BAH wing with CC

For the investigation of CC on the BAH wing, the NACA65A004 aerofoil section is replaced by NACA0012 aerofoil to allow for CC installation with reasonable thickness. As displayed in Ref. Bisplinghoff et al. (1996), the BAH wing has an aileron deployed from $\eta = y/l = 0.74$ to the wingtip. Based on this information, Coanda device with the similar length

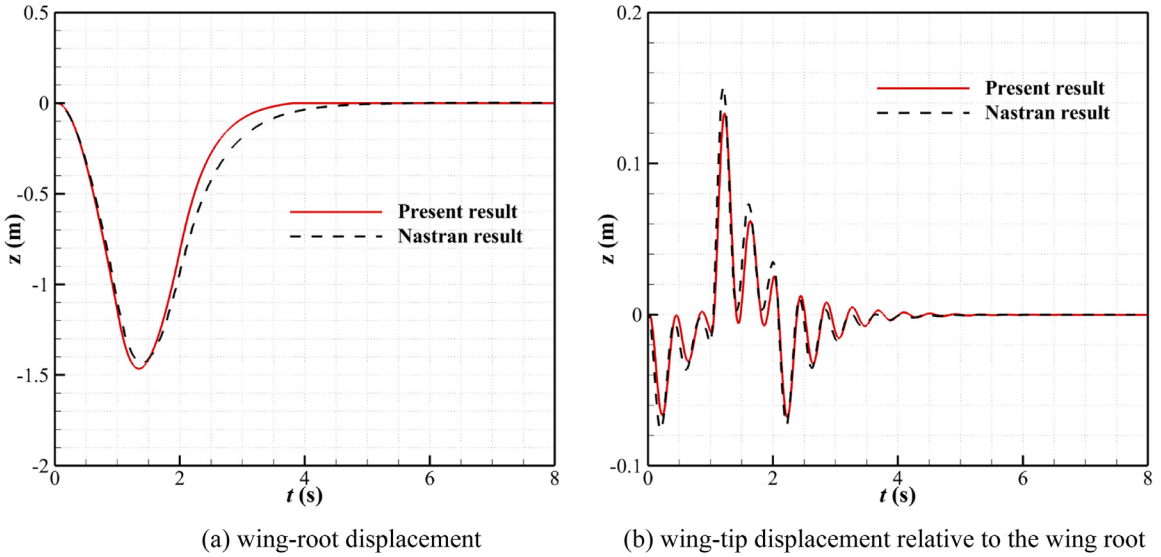


Fig. 5. Comparison of the real displacement responses.

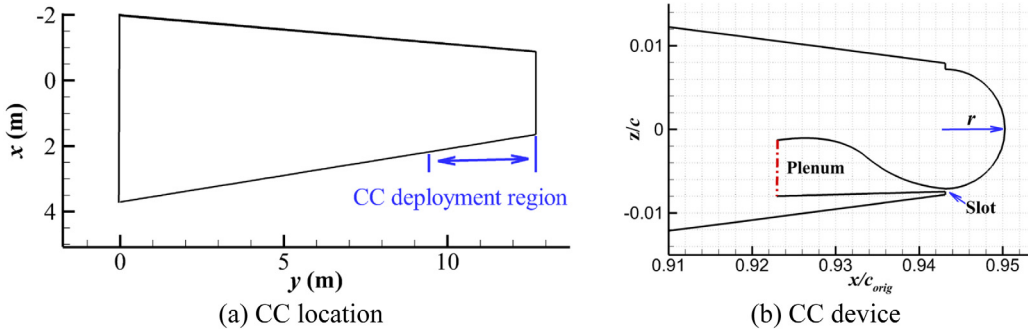


Fig. 6. The location of the CC on the BAH wing and the CC device.

in spanwise direction (from $\eta = y/l = 0.74$ to 0.98) is included on the BAH wing trailing edge as shown in Fig. 6. The CC deployment in the chord direction is shown in Fig. 6(b). The parameters of the Coanda device are the same as those used in the previous 2D aerofoil study in Ref. Li and Qin (2019) as shown here. The local aerofoil is truncated at $x/c_{\text{orig}} = 0.943$ (c_{orig} means the local chord length of the wing section before being truncated) and a semicircular trailing edge with a radius $r/c_{\text{orig}} = 0.714\%$ is added to the trailing edge. The ratio of the slot-exit height to the radius is 1:20. Fig. 6 (b) gives the detailed trailing-edge CC system. For the boundary conditions, no-slip condition is applied to the Coanda surface and the internal plenum surfaces. A reservoir boundary condition is used to set the desired total pressure and temperature. Here, the total pressure and temperature are fixed based on the assumption that the plenum air supply has been isentropically compressed. The momentum coefficient is calculated *a posteriori* by integrating the solution of the mass flow rate and jet velocity along the slot exit according to $C_\mu = \frac{\dot{m}U_{\text{jet}}}{q_\infty A}$, where \dot{m} is the mass flow rate, q_∞ is the freestream dynamic pressure, A is the surface area of the wing and U_{jet} is the jet velocity.

Based on the experience of grid resolutions for the simulations of CC presented in the previous study, a baseline grid is generated for simulations of CC on the BAH wing as presented in Fig. 7. The baseline mesh contains 221 cells on the wing aerofoil section, 149 cells in the wall-normal direction, 121 cells over the span and 121 cells on the Coanda surface. The total grid size is about 6.1×10^6 . From this, a coarser mesh and a finer mesh with a total number of cells of approximately 3.5×10^6 and 10.6×10^6 respectively, are generated to conduct the grid refinement study. The mesh refinement ratio between the coarse and medium grids in each direction is about 1.2 with a constant distance of the first grid point from the wall to keep the $y^+ \sim O(1)$.

Table 1 gives the effects of grid resolutions on the aerodynamic coefficients at $M = 0.7$, $\alpha = 3.0^\circ$ under a blowing momentum coefficient $C_\mu = 1.57 \times 10^{-4}$. The estimation of aerodynamic coefficients with an ‘infinite’ grid is performed using the Richardson extrapolation by $C_{\text{continuum}} = C_{10.6m} + \frac{(C_{10.6m} - C_{6.1m})}{(r^2 - 1)}$, where $r = 1.2$. It is noticeable that for the lift coefficient, the difference between the medium and the fine grids is less than 1%, and it is about 2.1% for the root bending

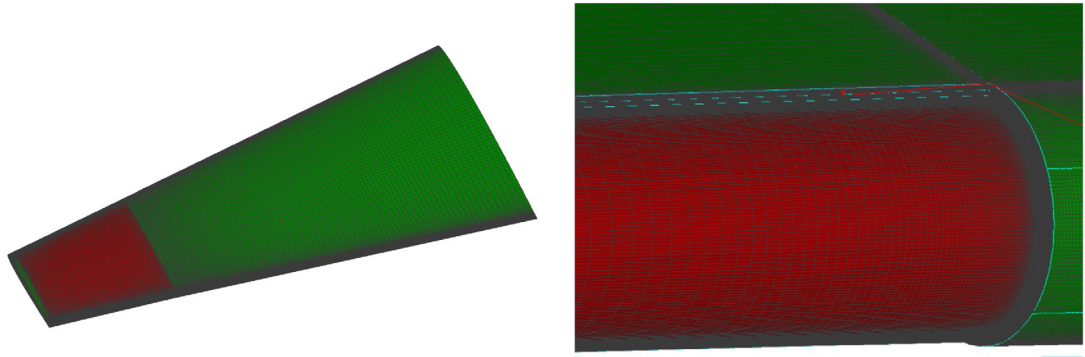


Fig. 7. Grid topology on the BAH wing and around the Coanda surface.

Table 1
Grid resolution effects on aerodynamic coefficients.

Grid size	3.5×10^6	6.1×10^6	10.6×10^6	Continuum
C_L	0.2819	0.2836	0.2856	0.2901
C_{mx}	0.1172	0.1190	0.1202	0.1229

moment coefficients (C_{mx}). The grid with 6.1×10^6 cells produces lift result that is within 2.1% of the continuum estimate, and it is less than 3.2% for the root bending moment coefficient. From these results, it was indicated that the medium grid gives reasonably accurate results while with computational cost efficiency.

4.2. Load control effects at steady condition

To get a quantitative knowledge of the load control capabilities of CC on the BAH wing, a series of computations at different momentum coefficients were conducted at $M_\infty = 0.3$, $\alpha = 3^\circ$, $Re_c = 4.13 \times 10^6$, and $M_\infty = 0.7$, $\alpha = 3^\circ$, $Re_{c_{ref}} = 2.06 \times 10^7$. The reduction of lift coefficients and root bending moment coefficients due to CC is shown in Fig. 8. For both Mach numbers, the reduction magnitudes in the lift and root bending moment coefficients increase with increasing momentum coefficients. The reduction magnitudes then decrease as the momentum coefficient reaches a critical value. This phenomenon is called ' C_μ stall' which describes the phenomenon that the change of aerodynamic forces due to CC will decline when momentum coefficients reach some extent due to the jet detachment (Cook et al., 2008; Wetzel et al., 2013). Also shown in the results is that the load control effects are stronger for the subsonic case compared with that at transonic speed. This is consistent with the CC characteristic demonstrated Refs. Alexander et al. (2005) and Li and Qin (2019). The reason for the difference may be explained from the mechanism for CC control. CC uses the entrainment by the high-speed jet flow following the Coanda surface to accelerate the external flow. Therefore, when the external flow velocity is lower for the subsonic case, CC has a stronger entrainment capability. On the other hand, when the incoming flow is transonic, the entrainment capability is more limited as the external flow velocity is closer to the jet flow velocity. To be specific, the momentum coefficient at ' C_μ -stall' is around 1.95×10^{-3} and 3.0×10^{-4} for $M_\infty = 0.3$ and 0.7 , respectively. A maximum reduction in lift coefficient of -0.15 is obtained under $M_\infty = 0.3$, while this value is only -0.032 at $M_\infty = 0.7$. The maximum reduction in root bending moment coefficients is -0.11 and -0.031 , respectively for these two Mach numbers.

Fig. 9 shows the Mach number counters on the slice of $\eta = 0.4$ and 0.87 , and the pressure coefficient distributions on the wing surface under $C_\mu = 8.1 \times 10^{-4}$ at $M_\infty = 0.3$ and $C_\mu = 3.0 \times 10^{-4}$ at $M_\infty = 0.7$. Compared to the streamlines shown at $\eta = 0.4$ where there is no CC deployment, the streamlines from the wing lower surface are entrained significantly upwards for the slice of $\eta = 0.87$ due to the high-speed CC jet flow. Due to the 'bend-up' of the jet flow streamlines, the flow near the upper trailing edge is hindered, resulting in the increase of the surface pressure on the upper trailing edge around the wing-tip region as shown in Fig. 9.

To evaluate the influence of CC on the whole spanwise load, the spanwise load distributions ($C_{local} c/c_{ref}$) are compared in Fig. 10 between the no-blowing case and the blowing case at $M_\infty = 0.3$ and 0.7 . From the comparisons, a more significant load control effect can be noticed around CC deployment region ($\eta = 0.74$ to 1.0). Also shown is that apart from this region, CC also has influence on the span load towards the wing root, but with a reducing load control effect.

4.3. Time step resolutions and dynamic actuation of CC jet

To get an appropriate time step for the simulation of dynamic CC, a transient actuation of CC is evaluated under $M_\infty = 0.3$, $\alpha = 3^\circ$ and $M_\infty = 0.7$, $\alpha = 3^\circ$. For this simulation, the model is initially at the converged steady-state flow.

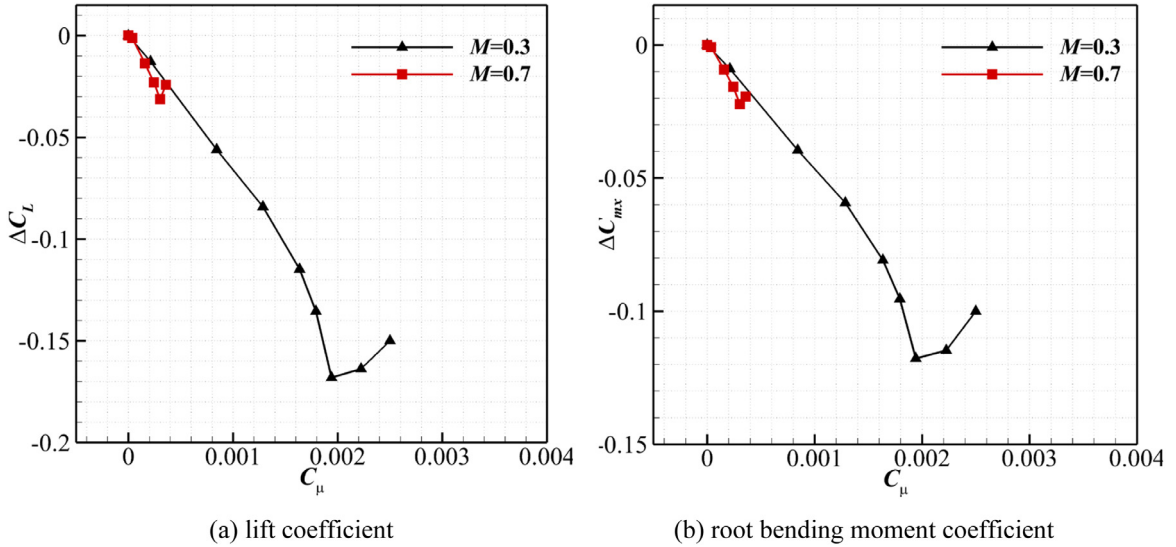
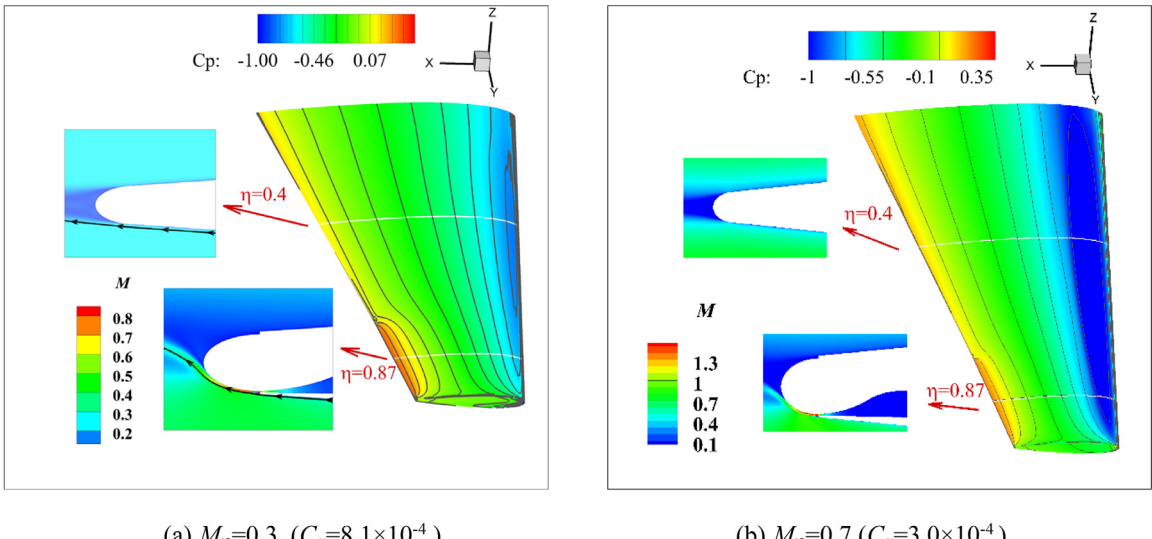
Fig. 8. Load control effects at steady conditions ($\alpha = 3^\circ$).

Fig. 9. The Mach number counter on typical slices and the pressure coefficient distribution on the wing surface.

CC jet is then activated at $s = 0$ to the maximum coefficient of $C_\mu = 1.28 \times 10^{-3}$ and $C_\mu = 2.9 \times 10^{-4}$ for $M_\infty = 0.3$ and 0.7, respectively. The non-dimensional time step Δs ranging from 7×10^{-4} to 7×10^{-3} is tested, and the results are shown in Fig. 11.

The results demonstrate that the difference in the lift responses from these three different time steps is negligible, especially for $\Delta s = 7 \times 10^{-4}$ and 1.4×10^{-3} . $\Delta s = 1.4 \times 10^{-3}$ is then chosen herein. Under different time steps, the lift coefficients all reach the same final steady-state value generally at around $s = 10$ after activating the CC jet. Also shown in the results is that sharp decrease of the lift coefficient due to CC happens at the first few non-dimensional time periods, indicating the fast response characteristic of CC. More than 50% of the total change in lift coefficient has been obtained within $s = 1$. This is consistent with the results in de Vries et al. (2009) of the experimental and numerical study about the load control effects of surface jet blowing on the NACA0018 aerofoil at $M_\infty = 0.176$.

Since gusts are dynamic disturbances featuring various frequencies, the performance of dynamic CC is the vital factor for its application in gust load alleviation, especially for high-frequency gusts. For the understanding of the behavior of the dynamic CC, the responses of CC with periodic actuations are evaluated at $M_\infty = 0.3$ and 0.7, $\alpha = 3^\circ$. The dynamic

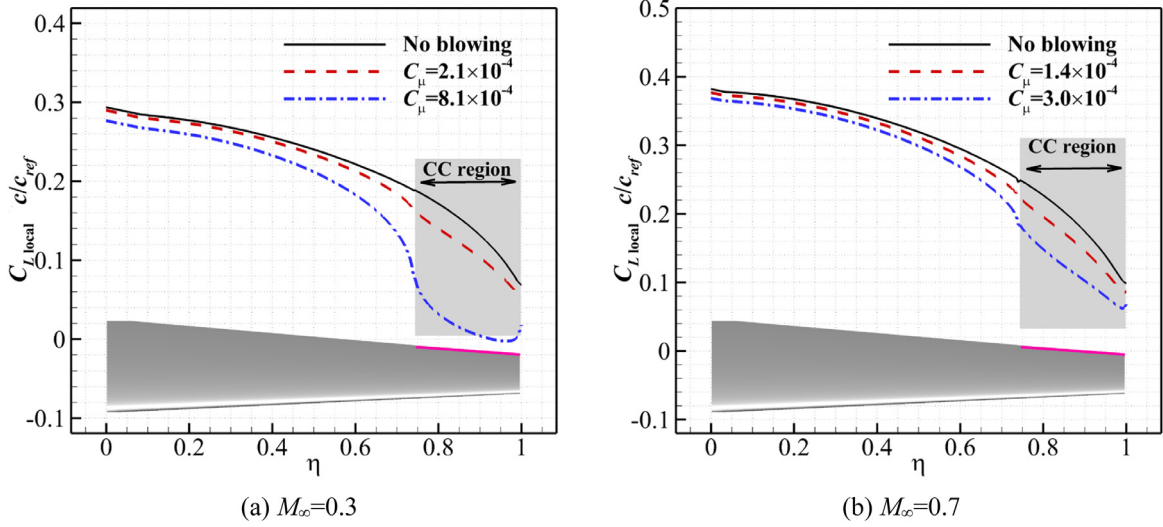


Fig. 10. The influence of spanwise load distributions due to CC jet blowing.

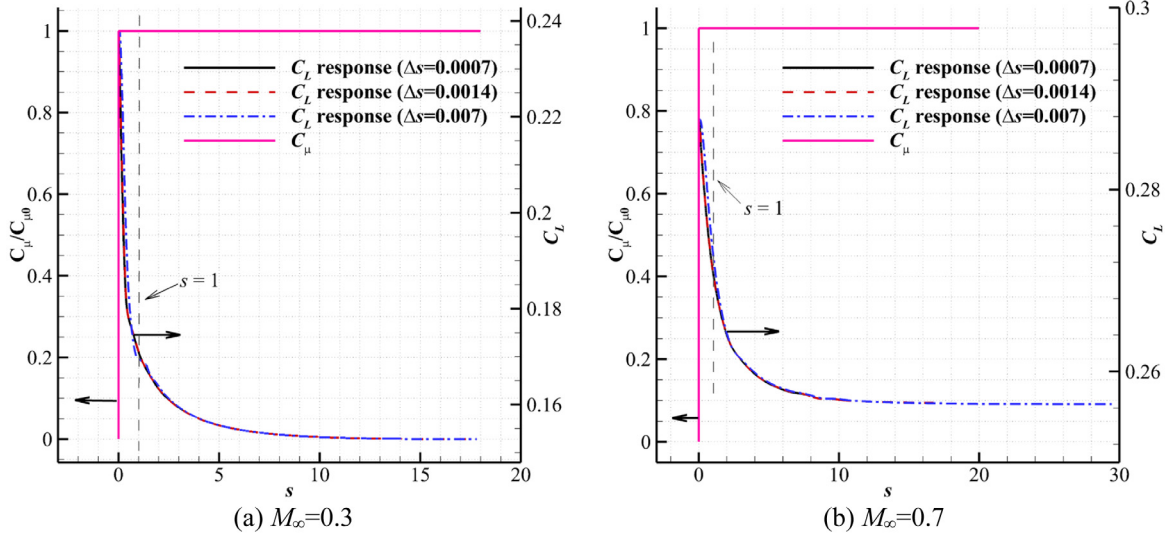


Fig. 11. Influence of the time steps.

CC momentum coefficient has the following form as:

$$C_\mu = C_{\mu 0} \cdot |\sin(2\pi f \cdot s)| \quad (4)$$

The reduced frequency is $k = \frac{\pi f c_{ref}}{U_\infty}$. In EASA CS-25 (Anon, 0000), the typical gust length is defined as $12.5c_{ref}$, corresponding to the reduced frequency of 0.25. To assess the effects of CC actuation frequency, three different reduced frequencies, $k = 0.125, 0.25, 0.5$ are tested herein with the maximum momentum coefficient $C_{\mu 0}$ of 1.28×10^{-3} for $M_\infty = 0.3$ and 2.9×10^{-4} for $M_\infty = 0.7$, respectively. To impose the unsteady momentum coefficient, simulations for a series of steady pressure ratios were firstly conducted. The corresponding momentum coefficients were calculated for each pressure ratio. A list of correspondence between the momentum coefficients and pressure ratio was built up. Based on the relationship, the unsteady pressure ratio is interpolated for the desired unsteady momentum coefficient and imposed as the boundary condition.

The results are shown in Fig. 12 in the forms of hysteresis loops for the lift responses against the changes in CC momentum coefficient. All loops are clockwise. For both Mach numbers, the hysteresis loops start with a small positive slope. This is because the momentum coefficient starts from zero initially, thus the CC jet-flow velocity also starts from zero. At the very beginning, when the momentum coefficient is too small, the CC jet-flow velocity is too small to attach

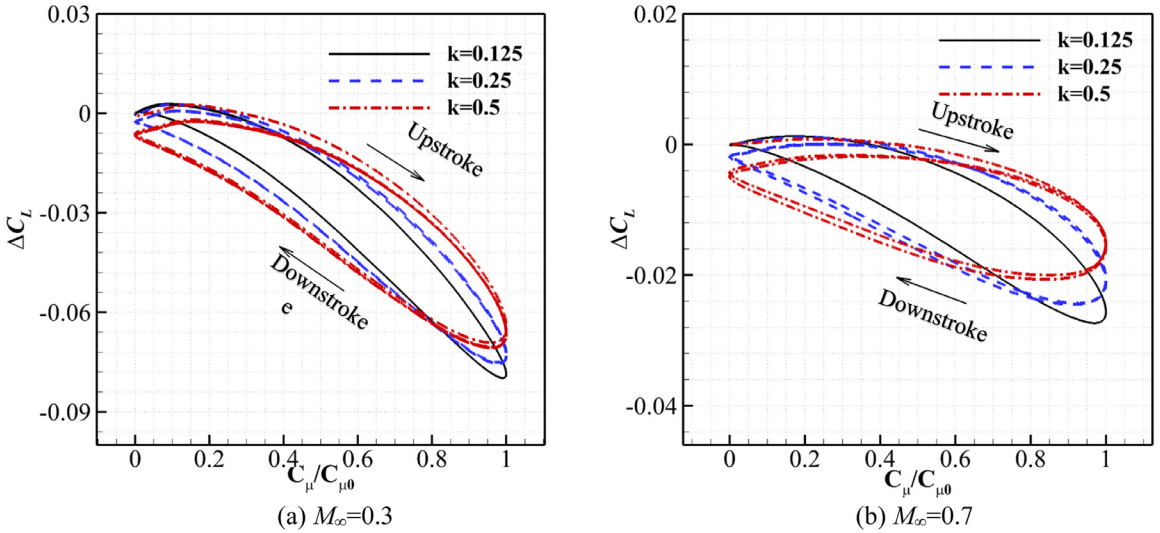


Fig. 12. Lift response with dynamic actuation of CC.

on the Coanda surface. These slopes quickly change to be negative demonstrating effective increasing load control ability with increasing blowing momentum coefficients. The slopes decrease slightly with the increasing reduced frequency at $M_\infty = 0.3$. This indicates the reduction of load control effects with increasing frequency of unsteady CC-jet blowing. This phenomenon becomes more apparent under $M_\infty = 0.7$ compared to that at $M_\infty = 0.3$ as shown in Fig. 12 (b), as more significant decrease in the slope with increasing frequency has been noticed. This is substantially related to the inherent weakness of CC entrainment under transonic flow demonstrated in Refs. Li and Qin (2019).

5. BAH wing gust load alleviation by CC

5.1. Subsonic case study at $M_\infty = 0.3$

For the certification specifications of large commercial aircraft, EASA CS-25 (Anon, 0000) defined a typical discrete gust as the ‘one-minus-cosine’ gust. According to EASA CS-25, the gust wavelength is in the range from 9 to 107 m. In practice, the typical value is $12.5c_{ref}$ (c_{ref} is the mean aerodynamic chord length), which is 51.6 m for the BAH wing (Bisplinghoff et al., 1996).

The gust velocity w_{g0} changes with gust wavelength and altitude which is expressed in relations of the gust gradient (half of the gust wavelength) H_g (in m), the flight profile alleviation factor F_g and the reference gust velocity w_{ref} , as

$$w_{g0} = w_{ref} F_g \left(\frac{H_g}{106.17} \right)^{\frac{1}{6}} \quad (5)$$

where, w_{ref} decreases linearly from 17.07 m/s equivalent airspeed (EAS) at sea level to 13.41 m/s at 4572m altitude and then again to 6.36 m/s at 18,288 m altitude. The flight profile alleviation factor F_g increases linearly from the sea level value up to a value $F_g = 1$ at the maximum operating altitude.

For $M_\infty = 0.3$, considering the BAH wing flies at sea level, the gust velocity is set to be 6.74 m/s assuming $F_g = 0.5$ corresponding to a maximum gust-induced angle of attack ($\tan^{-1}(\frac{w_g}{U_\infty})$) of about 3.8° . Eq. (6) expresses the profile of the ‘one-minus-cosine’ gust in the non-dimensional time domain. The gust response simulation starts from $s = 0$ when the gust front point encounters the leading edge of the root wing section. The gust then proceeds by traveling past the wing with the same velocity as the incoming flow. Initially, the BAH wing is flying at the convergent flow condition with the angle of attack of $\alpha = 3^\circ$.

$$\begin{cases} w_g = 0 & s < 0 \\ w_g = \frac{1}{2} w_{g0} \left(1 - \cos \frac{2\pi s}{12.5} \right) & 0 \leq s \leq 12.5 \\ w_g = 0 & s > 12.5 \end{cases} \quad (6)$$

Fig. 13 shows the responses of lift and root bending moment coefficients to the gust. After the gust hits the root-chord leading edge at $s = 0$, the lift and root bending moment coefficients increase as the gust proceeds. The lift and root bending moment coefficients peak at around $s = 6.7$. To be specific, the peak gust load caused a maximum increase of

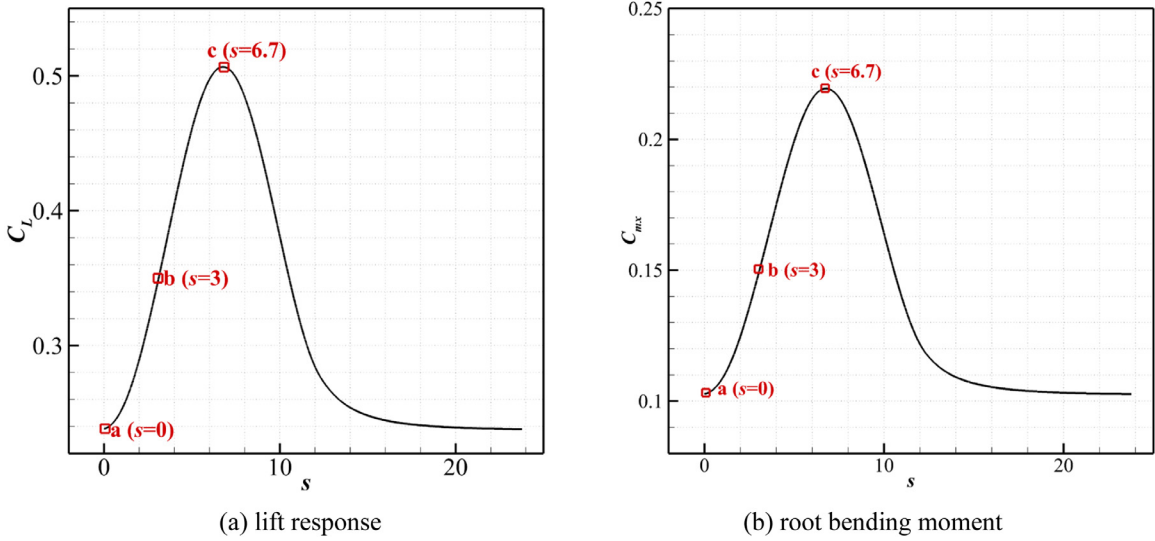


Fig. 13. Responses of lift and root bending moment coefficients to the gust of the BAH wing at $M_{\infty} = 0.3$.

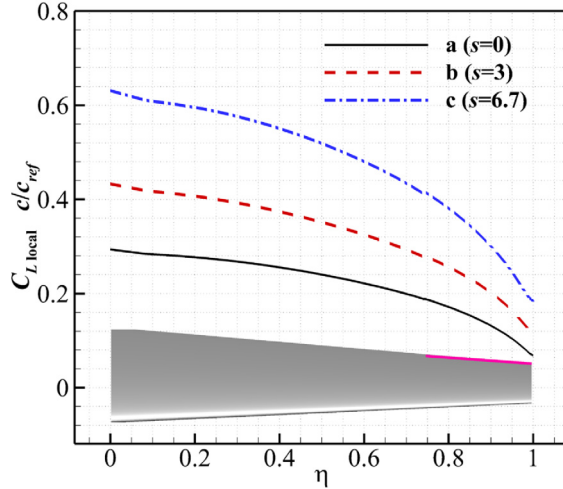


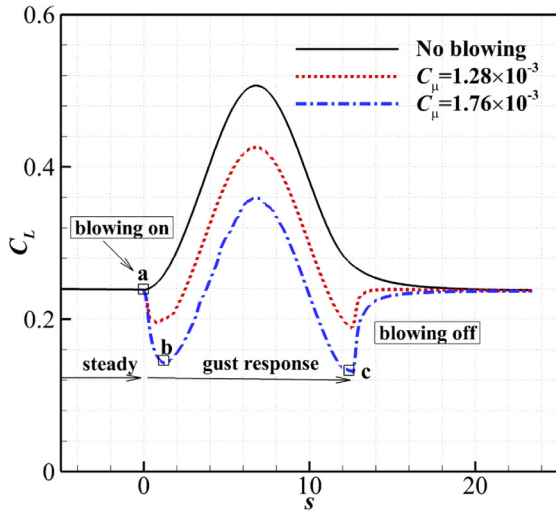
Fig. 14. Evolution of the spanwise loading to the gust at $M_{\infty} = 0.3$.

lift and root bending moment coefficients to around $C_L = 0.5$ and $C_{mx} = 0.22$, respectively. These peak values are more than twice the initial values which are $C_L = 0.238$ and $C_{mx} = 0.102$ at $s = 0$. Three specific points in time are labeled from $s = 0$ to $s = 6.7$, and the corresponding evolutions of the spanwise loading are shown in Fig. 14. As shown in the results, significant load increases have been observed along the whole span with the increase in gust load.

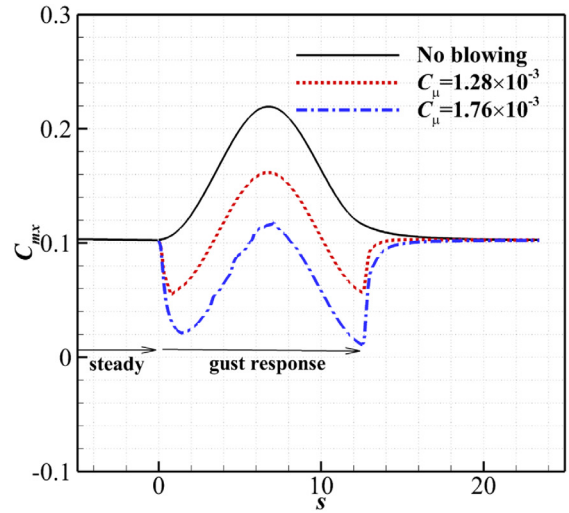
5.1.1. CC with constant blowing momentum coefficients on the rigid wing

Firstly, to demonstrate the gust load alleviation effects, CC with constant blowing momentum coefficient is tested. During the process, CC jet is activated at the initial time $s = 0$ to the prescribed momentum coefficient and this is kept constant until $s = 12.5$ when the jet blowing is turned off. As demonstrated in the previous load control capability studies at steady states, the ' C_{μ} stall' is at around $C_{\mu} = 1.95 \times 10^{-3}$ at $M_{\infty} = 0.3$. This study does not consider the investigation of the momentum coefficient above the critical value. Two different values of the momentum coefficient $C_{\mu} = 1.28 \times 10^{-3}$ and 1.76×10^{-3} are applied for this demonstration.

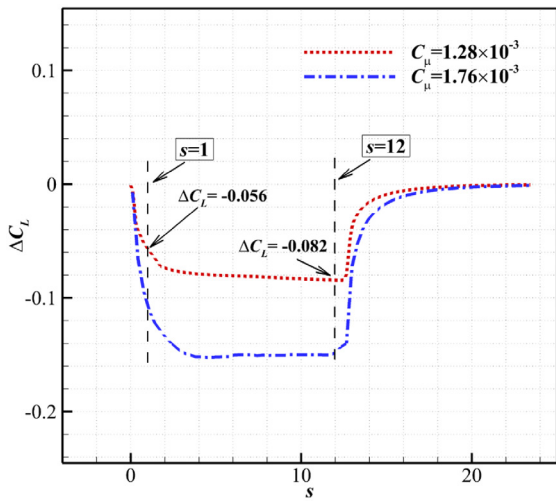
The results of the evolution of lift and root bending moment coefficients under the gust are compared between the CC models and the baseline model as shown in Fig. 15. The jet blowing is turned on at $s = 0$ (point *a* in Fig. 15) when the gust hits the leading edge of the root wing section. From both responses of the lift and the root bending moment, a sharp decrease from the initial point *a* to point *b* ($s \approx 2$) can be noticed for cases with CC.



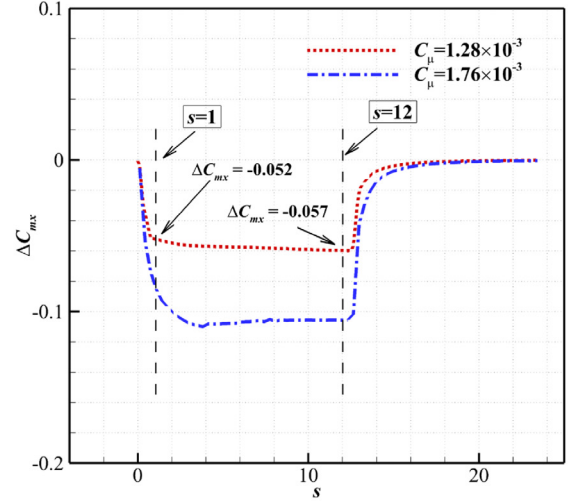
(a) lift coefficient



(b) root bending moment coefficient

Fig. 15. Gust alleviation characteristic to one-minus-cosine gust with constant blowing at $M_\infty = 0.3$.

(a) lift coefficient



(b) root bending moment coefficient

Fig. 16. Relative load reduction with constant blowing to the baseline model at $M_\infty = 0.3$.

Fig. 16 presents the reductions of the lift and root bending moment coefficients of these two blowing cases relative to the unblown case. From the results, it can be seen that more than 50% of the total change in the load due to CC can be obtained within the non-dimensional time $s = \frac{U_\infty t}{C_{ref}}$. This results in a sharp decrease in the total load response. Point c is the moment when the gust trailing point touches the wing root leading edge and the CC jet is turned off. From this point onwards, the lift and root bending moment coefficients increase sharply due to the loss of the control by CC. Afterwards, these coefficients under different CC conditions generally return to the same initial values as the gust passes downstream. Even though, it is clearly demonstrated that the peak gust loads in terms of no matter lift or root bending moment coefficients have been alleviated significantly, the responses of these loads still have large fluctuations under the gust perturbations. This demonstration indicates that CC with constant blowing momentum coefficients can significantly alleviate the peak gust loads but cannot properly control the loads fluctuations under the gust conditions. It is expected that dynamically adjusting the momentum coefficient is needed for a better control of the gust load fluctuations. To this end, a straightforward way is to use unsteady CC jet blowing by adjusting the momentum coefficients proportionally to the gust velocity variation.

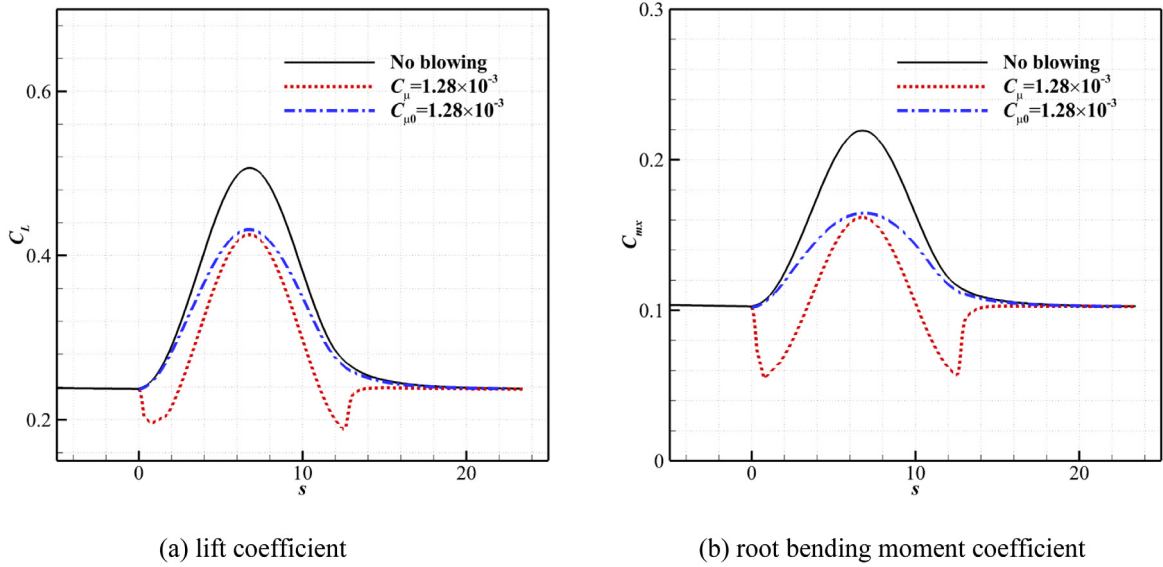


Fig. 17. Load control effects with constant and unsteady blowing at $M_\infty = 0.3$.

5.1.2. CC with unsteady blowing momentum coefficients on the rigid wing

To get an insight into the responses of unsteady CC blowing in the gust load alleviation process, the same profile of the momentum coefficients in the time domain as that of the gust velocity is tested. This profile can be expressed as the following equation.

$$\begin{cases} C_\mu = 0 & s < 0 \\ C_\mu = \frac{1}{2} C_{\mu 0} \left(1 - \cos \frac{2\pi s}{12.5} \right) & 0 \leq s \leq 12.5 \\ C_\mu = 0 & s > 12.5 \end{cases} \quad (7)$$

where, $C_{\mu 0}$ is the peak value of the unsteady momentum coefficients. Firstly, the peak momentum coefficient of $C_{\mu 0} = 1.28 \times 10^{-3}$ is tested and compared with the previous constant blowing with $C_\mu = 1.28 \times 10^{-3}$. From the responses of the lift and root bending moment coefficients shown in Fig. 17, it can be seen that both the unsteady blowing and the constant blowing can achieve significant peak gust load alleviation. However, compared to the constant blowing, the unsteady blowing has a better control of the gust load disturbances.

The peak momentum coefficient of the unsteady blowing is then increased to 1.76×10^{-3} . As shown in Fig. 18, CC with $C_{\mu 0} = 1.76 \times 10^{-3}$ achieved a further gust load reduction compared to $C_{\mu 0} = 1.28 \times 10^{-3}$. To be specific, CC with $C_{\mu 0} = 1.76 \times 10^{-3}$ reduced the peak lift coefficient by approximately 44%, with the alleviation in lift coefficient from 0.268 to 0.117. For the root bending moment, the peak value is reduced by 71% for CC with $C_{\mu 0} = 1.76 \times 10^{-3}$. It can be seen that CC achieved more relative reduction in root bending moment (71%) than that in lift (44%). It is because CC is deploying around the wingtip where the variation of the load will have a significant influence on the root bending moment due to the long moment arm. This can also be demonstrated from the comparisons of the spanwise load distributions (Fig. 19) between these three models at the initial time $s = 0$ and $s = 6.7$ when the gust load peaks. A significant load reduction can be observed around the wing-tip region for the CC models compared with the baseline one. The load control effect is so significant that for the CC models with $C_{\mu 0} = 1.28 \times 10^{-3}$ and 1.76×10^{-3} , the load around the wing-tip area under the peak gust load at $s = 6.7$ is alleviated to be even lower than that at the initial time. Therefore, assuming CC is deployed along the whole span, the gust load can be completely alleviated.

5.1.3. CC with unsteady blowing momentum coefficients on the elastic wing

In this case study, the plunging mode and the first bending elastic mode which are the same as those used in the verification study are included in the gust load responses. Under the same gust condition as that used in the previous case study, the gust responses in terms of lift and root bending moment coefficients of the baseline (unblown) models are compared between the rigid and elastic wings as shown in Fig. 20. The gust response simulations are initialized from the converged steady-state flow. The gust hits the root-chord leading edge at $s = 0$ and travels past the wing to the downstream farfield. That is why the lift and root bending moment coefficients increase as the gust proceeds and peaks at around $s = 6.7$ when the peak gust load travels past the root-chord leading edge. As the gust passes through the wing to the downstream farfield, the lift and root bending moment coefficients recover slowly with a long time duration

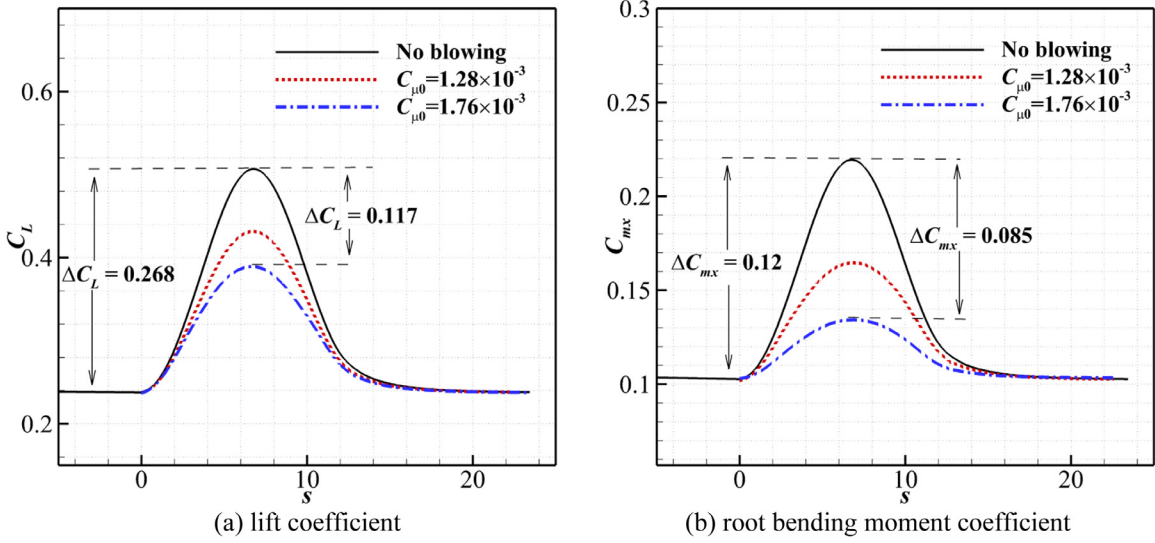


Fig. 18. Load control effects with an unsteady jet blowing under gust condition at $M_\infty = 0.3$.

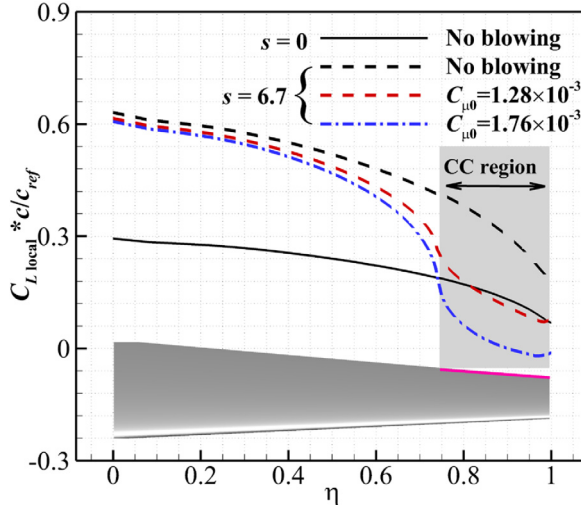
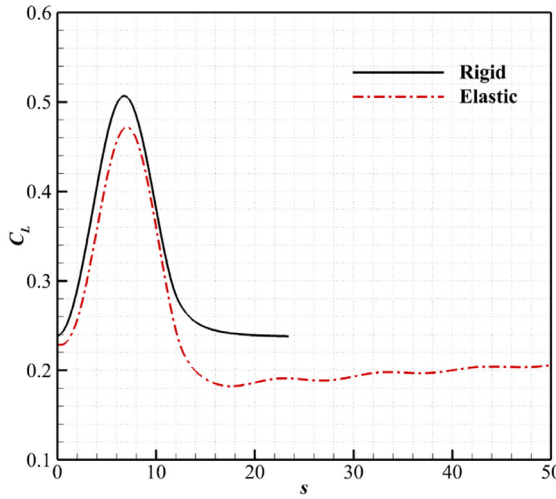


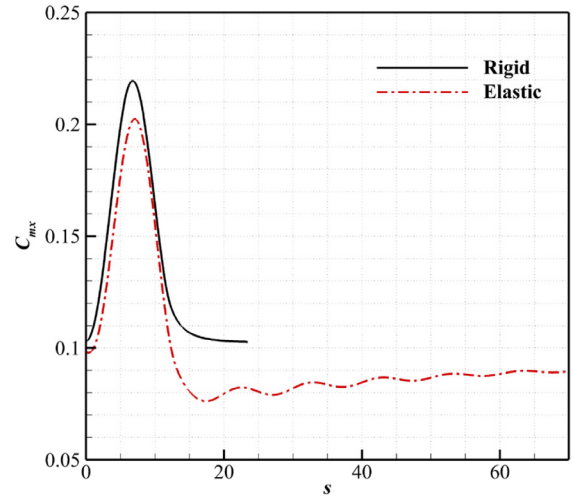
Fig. 19. Comparisons of the spanwise load distributions at $M_\infty = 0.3$.

compared to the initial responses as the gust hits the wing. From the results, significant differences in the responses can be noticed between the rigid and elastic wings. Firstly, due to the influence of the static elasticity, the initial values of the lift and bending moment coefficients of the elastic wing are slightly smaller relative the rigid wing. It is also noticed that the peak gust load of the elastic wing is also smaller than that of the rigid wing. This is because of the alleviation of the gust load from the plunging motion and the elastic deformation of the elastic wing. Another significant difference between the rigid and elastic wings is the gust-response period. For both wings, the gust traveled past the wing at the same time of $s = 13.9$ (the gust wavelength plus the wing-root length is $13.9c_{\text{ref}}$). For the rigid model, the lift and the root bending moment responses caused by gust decay at around $s = 16$ which is slight longer than $s = 13.9$ as the gust needs time to pass far away from the wing to where the gust disturbances have little influence to the aerodynamic forces of the wing. However, for the elastic model, the aerodynamic forces see oscillations in the time history, and it takes longer time to recover to the initial state. As shown in Fig. 20, after the gust travels past the wing, the aerodynamic forces gradually return to the initial steady-state values with small oscillations due to the structural vibrations caused by aeroelasticity.

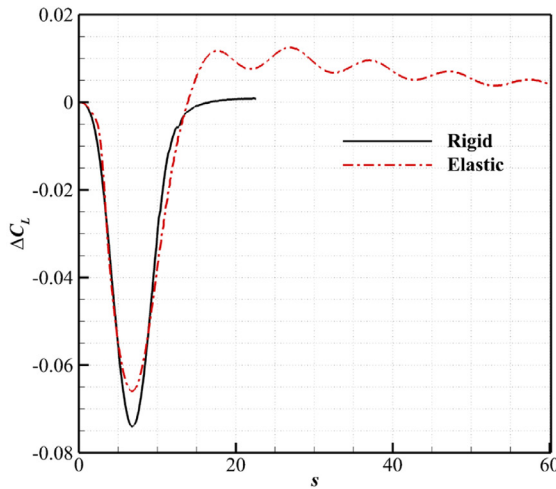
The peak momentum coefficient of $C_{\mu 0} = 1.28 \times 10^{-3}$ is firstly tested for the gust load alleviation on the elastic wing and compared with that on the rigid wing. The reductions in lift and root bending moment coefficient due to CC relative to the baseline model are compared between the rigid and elastic wings as shown in Fig. 21. From the results, it can be seen that no matter it is rigid or elastic, CC has the capability for gust load alleviation. With the same unsteady blowing



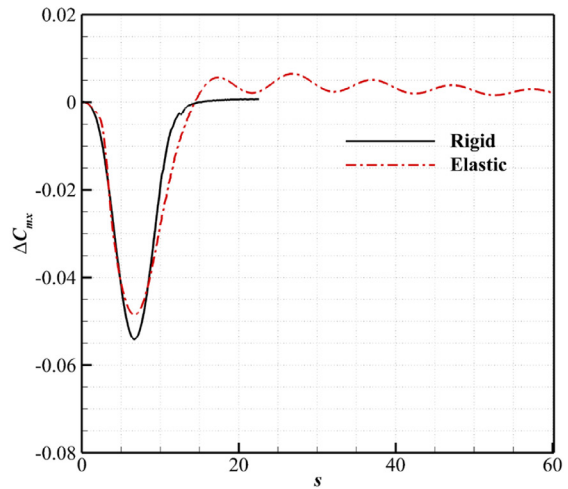
(a) lift coefficient



(b) root bending moment coefficient

Fig. 20. The time evolutions of the lift and root bending moment coefficients of the baseline rigid and elastic models at $M_\infty = 0.3$.

(a) lift coefficient



(b) root bending moment coefficient

Fig. 21. The gust load alleviation in terms of the reduction of lift and root bending moment coefficients on the rigid and elastic wings at $M_\infty = 0.3$.

momentum coefficient, a reduced gust load alleviation effect around the peak gust load has been noticed on the elastic wing compared to the rigid model. As for the elastic wing with plunging motion, the wing moves up during the gust encountering process which introduces an opposite velocity component to the CC jet flow, resulting in a slight reduction in load control effect.

The peak momentum coefficient of the unsteady blowing is then increased to 1.76×10^{-3} . As shown in Fig. 22, similar to the rigid model, CC with $C_{\mu 0} = 1.76 \times 10^{-3}$ achieved a further gust load reduction compared to $C_{\mu 0} = 1.28 \times 10^{-3}$. To be specific, the peak lift and root bend moment coefficients caused by gust of the baseline model have been reduced by 43% and 72% respectively for the model with $C_{\mu 0} = 1.76 \times 10^{-3}$. These relative values in lift and bending moment coefficient reduction are close to that demonstrated on the rigid wing which are 44% in lift and 71% in root bending moment, respectively.

The time evolutions of the vertical displacement on the wing-tip leading edge for the plunging mode and the first bending mode are presented in Fig. 23. For the baseline model with no blowing, the plunging displacement reaches around 1.8 m at $s = 100$. With CC, a significant reduction in the vertical displacement is obtained for both blowing cases. To be

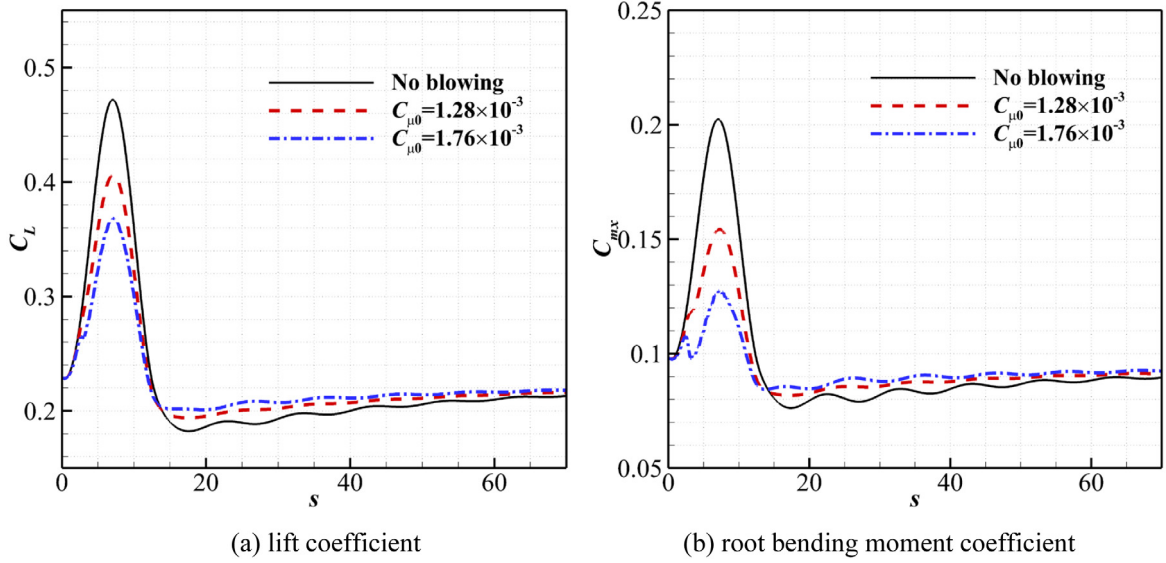


Fig. 22. The time evolutions of the lift and root bending moment coefficients on the elastic wing at $M_\infty = 0.3$.

specific, the displacements are reduced to 1.33 m and 1.07 m respectively for the model with $C_{\mu 0} = 1.28 \times 10^{-3}$ and 1.76×10^{-3} .

Compared to the plunging mode, the displacement of the elastic mode in the wing-tip leading edge is relatively small. Also shown is that the displacement of the elastic mode is sensitive to the CC momentum coefficient. For the baseline model, the initial vertical displacement of the elastic mode is upwards. It is because the wingtip feels an upward force when the wing initially encounters the gust. When the CC jet is deployed with $C_{\mu 0} = 1.28 \times 10^{-3}$, the direction of the initial motion is the same as the baseline model, but with a reduction in the magnitude due to the alleviation of the gust load. However, when the momentum coefficient increases to 1.76×10^{-3} , the initial motion becomes downwards. It is because the gust load on the outer wing sections where CC was deployed is further controlled and the normal force introduced by CC is larger than that caused by the gust, resulting in a downward force in the wingtip section. For the baseline model, the vertical displacement of the elastic mode reaches a maximum value of about 0.065 m at $s = 13.4$, while it is around 0 m and -0.04 m for the model with $C_{\mu 0} = 0.00128$ and 0.00176 , respectively. Fig. 24 shows the comparison of the wing displacements between the baseline model and the model with $C_{\mu 0} = 1.28 \times 10^{-3}$ at $s = 6.7$ and 100. At $s = 6.7$, the difference of the wing-tip deformation between these two models can be noticed. At $s = 100$, the larger vertical displacement of the baseline model than the model with $C_{\mu 0} = 1.28 \times 10^{-3}$ is clearly demonstrated. This indicates the significant suppression of the displacement by CC. Also shown in Fig. 23(b) is that with the gust load alleviation by CC, the oscillation of the first bending mode displacement decays much faster than the baseline model.

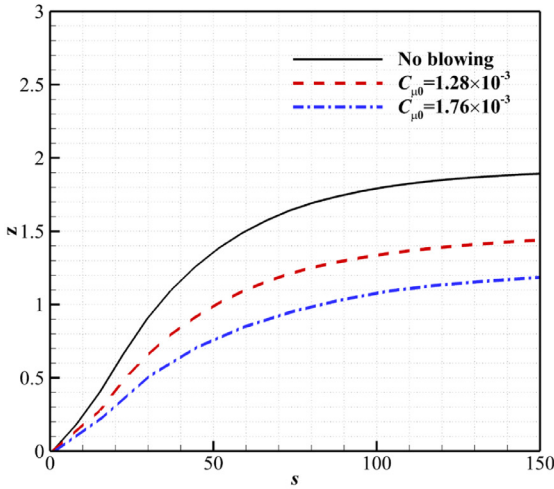
5.2. Transonic case study at $M_\infty = 0.7$

For $M_\infty = 0.7$, the gust wavelength is set to be $12.5c_{ref}$ with an estimated gust velocity of 5.85 m/s. The ' C_μ stall' is around 3.0×10^{-4} at the steady state of $M_\infty = 0.7$, $\alpha = 3^\circ$ as shown in Fig. 8. Two different peak momentum coefficients of $C_{\mu 0} = 2.5 \times 10^{-4}$ and 2.8×10^{-4} are chosen for the gust load alleviation study firstly on the rigid BAH wing.

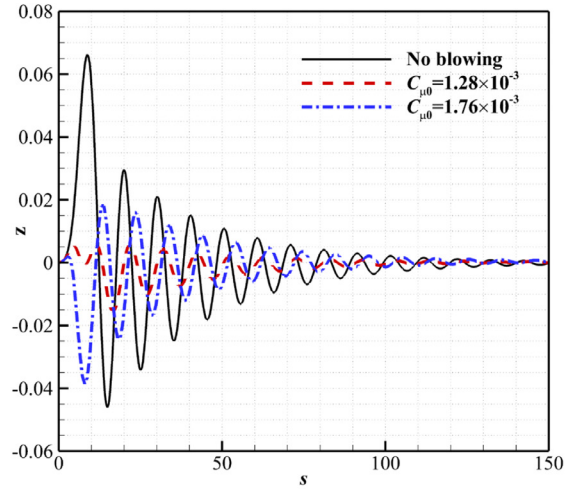
The gust responses in terms of lift and root bending moment coefficients with these two blowing conditions and the unblown case are shown in Fig. 25. Like the results in the subsonic case studies at $M_\infty = 0.3$, CC is capable for gust load alleviation. For CC with $C_{\mu 0} = 2.8 \times 10^{-4}$, an alleviation of the peak of 33% due to CC can be noticed on lift, and 53% on the root bending moment. These achievements in load reduction are smaller compared to the values obtained by CC under subsonic cases demonstrated in the previous section.

Fig. 26 shows the comparisons of the spanwise load distributions among these three models at the initial time $s = 0$ and $s = 7$ when gust load peaks. Under the peak gust load, the whole spanwise load of the baseline model increases significantly compared to that at the initial time. With CC jet blowing, the spanwise load is noticeably alleviated, especially around the wing-tip region. For CC with $C_{\mu 0} = 2.8 \times 10^{-4}$, the gust load around the wing-tip region is completely suppressed at $s = 7$.

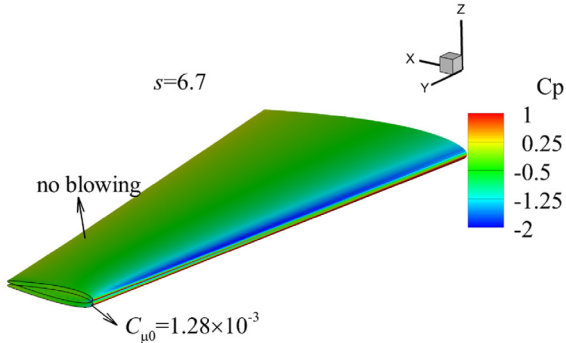
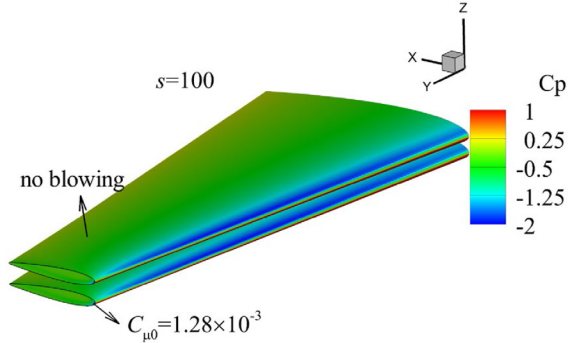
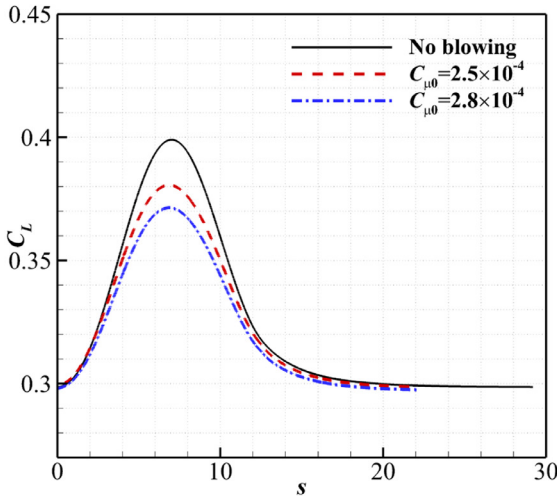
Then, the plunging and the first bending modes are included in the gust response. The gust and the CC blowing momentum coefficients are kept the same. Fig. 27 shows the resulting time evolutions of the lift and root bending moment coefficients. Alleviation of the peak of 31% has been achieved on lift, and 54% on the root bending moment for CC with $C_{\mu 0} = 2.8 \times 10^{-4}$ which are similar to the values obtained in the previous rigid case.



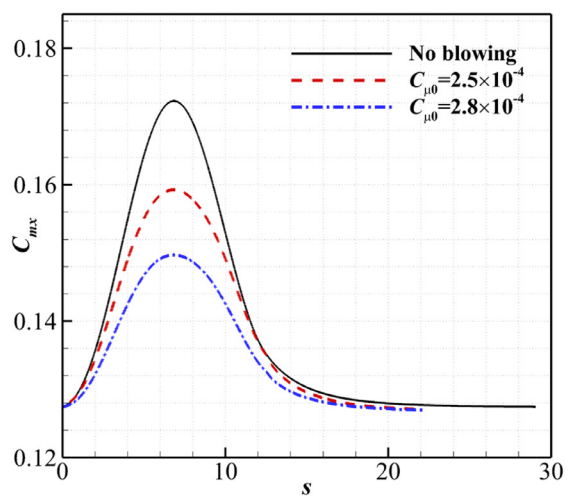
(a) plunging mode



(b) the first bending mode

Fig. 23. The vertical displacement of the leading edge of the wing-tip section at $M_\infty = 0.3$.(a) $s=6.7$ (b) $s=100$ **Fig. 24.** Surface pressure distribution and wing displacements at $M_\infty = 0.3$.

(a) lift coefficient



(b) root bending moment coefficient

Fig. 25. The time evolutions of the lift and root bending moment coefficients at $M_\infty = 0.7$.

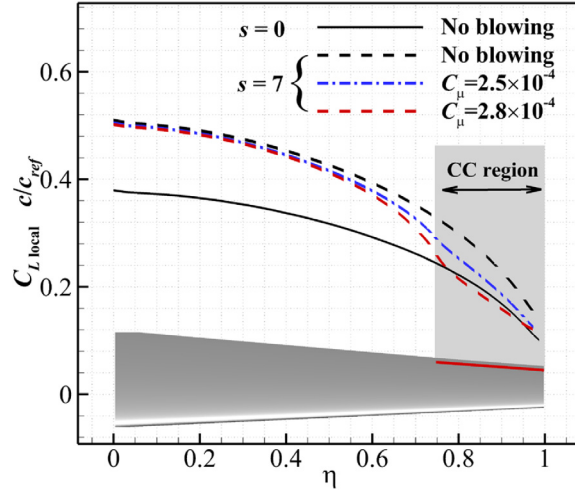


Fig. 26. Comparisons of the spanwise load distributions at $M_\infty = 0.7$.

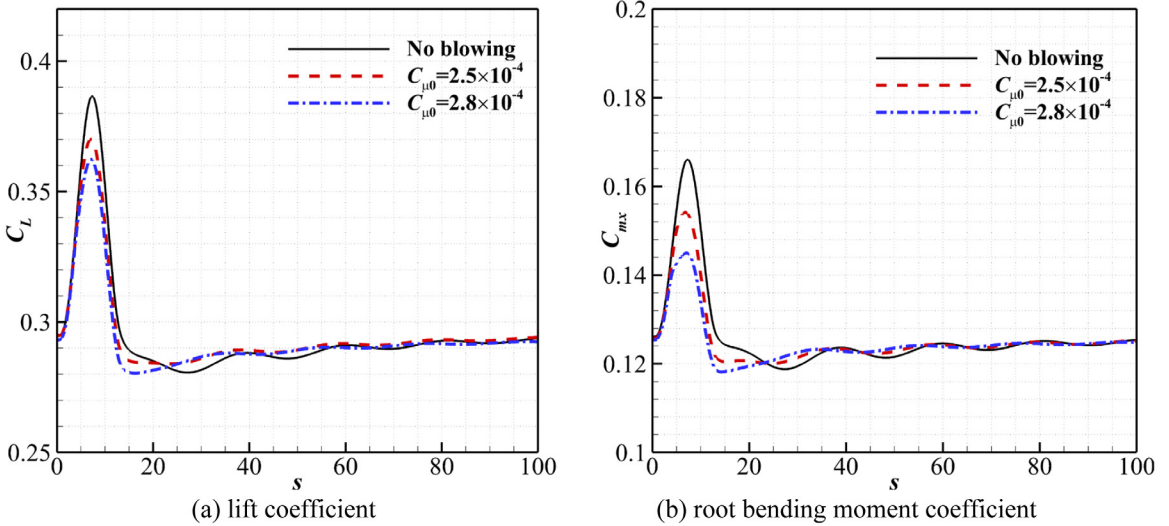


Fig. 27. The time evolutions of the lift and root bending moment coefficients at $M_\infty = 0.7$.

Fig. 28 represents the time evolutions of the plunging and the first elastic bending displacements. The application of CC induces a great decrease of the main peak of the first bending displacement (83% for CC with $C_{\mu 0} = 2.8 \times 10^{-4}$). The amplitude of the displacement oscillations for the models with CC is strongly damped compared to the baseline one. Like the elastic displacement, the plunging displacement is also alleviated by CC.

6. Conclusions

The feasibility and effect of gust load alleviation by means of circulation control are numerically studied on the BAH wing. The methods coupling Field Velocity Method, structural dynamic equations of motion and URANS solutions are validated for simulation of gust responses. The BAH wing is first modified to include the Coanda devices around the wing-tip trailing edge from $\eta = 0.74$ to 1.0. This is followed by the evaluation of the load control effects by constant and dynamic blowing momentum coefficients under steady incoming flow at $M_\infty = 0.3$ and 0.7. Gust load alleviation effects of the BAH wing are then tested under the typical 'one-minus-cosine' gusts defined by EASA CS-25. Both rigid and elastic BAH wing are considered in the test cases.

The evaluation of load control effects by CC on the BAH wing at steady condition demonstrates that CC has the capability for load control from subsonic to transonic incoming flows. The load control effect is much stronger under subsonic flow than that of transonic range. Apart from a significant load control effect around the span region where CC is deployed, CC also has influence on decreasing the spanwise load towards the wing root.

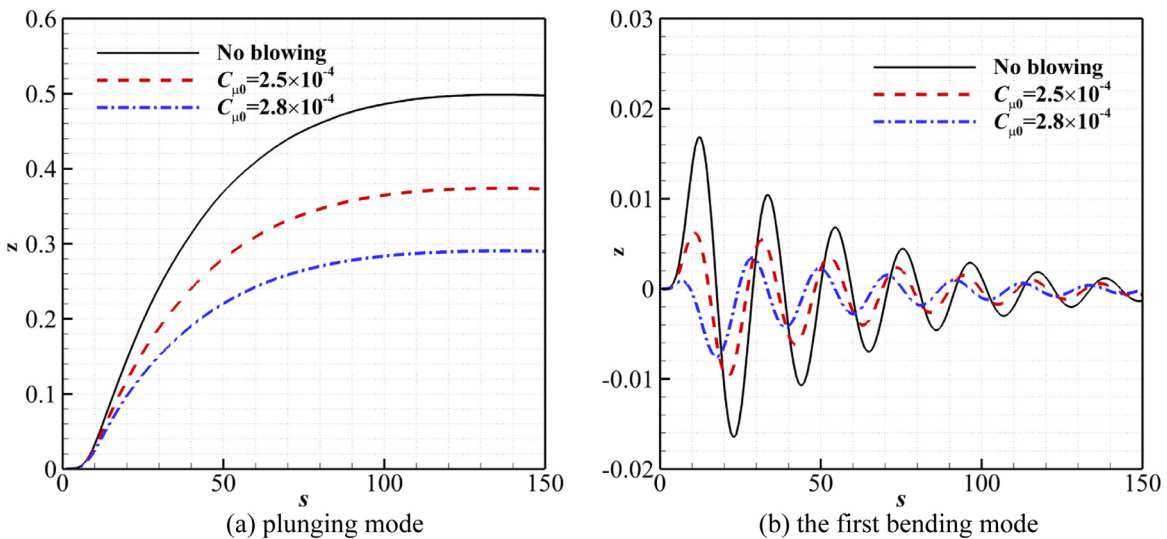


Fig. 28. The vertical displacement of the leading edge of the wing-tip section at $M_{\infty} = 0.7$.

The results of the transient actuation of CC demonstrate that a sharp decrease of the lift coefficient happens at the first few non-dimensional time periods, indicating the fast response characteristic of CC. More than 50% of the total change in lift coefficient has been obtained within $s = 1$. For dynamic actuation of CC, a decrease in load control effect with the increase in reduced frequency is observed.

The results of gust load alleviation verify that CC is able to suppress the gust load disturbances. For the test cases of both rigid and elastic BAH wing, a significant reduction in lift and root bending moment coefficients caused by gusts has been achieved. Under the same gust disturbances, the elastic wing has a smaller peak gust load due to the gust load alleviation from plunging motion and elastic deformation compared to the rigid model. The relative values in gust load alleviation are similar for the rigid and elastic wings under the same blowing momentum coefficient. Because of the alleviation in gust load due to CC, significant suppression of the disturbances in the displacement has been noticed in the case studies on the elastic BAH wing.

Declaration of competing interest

The authors declare that they have no known competing financial interests or personal relationships that could have appeared to influence the work reported in this paper.

Acknowledgments

The authors would like to acknowledge the support from the University of Sheffield Computing Service for HPC provision to conduct the research. The first author would like to acknowledge a studentship from CARDC China to support his PhD study.

References

- Al-Battal, N., Cleaver, D., Gursul, I., 2018. Lift reduction by counter flowing wall jets. *Aerosp. Sci. Technol.* 78, 682–695.
- Albano, E., Rodden, W.P., 1969. A doublet-lattice method for calculating lift distributions on oscillating surfaces in subsonic flows. *AIAA J.* 7 (2), 279–285.
- Alexander, M.G., Anders, S.G., Johnson, S.K., Florance, J.P., Keller, D.F., 2005. Trailing Edge Blowing on a Two-Dimensional Six-Percent Thick Elliptical Circulation Control Airfoil up to Transonic Conditions - NASA/TM-2005-213545. Sponsoring Organization: NASA Langley Research Center.
- Anon, ., 0000. EUROPEAN AVIATION SAFETY AGENCY - Certification Specifications for Large Aeroplanes CS-25.
- Anonymous, ., 2006. BAE Systems success in flapless flight. *Aircr. Eng. Aerosp. Technol.* 78 (2).
- Bartels, R.E., 2012. Development, Verification and Use of Gust Modeling in the NASA Computational Fluid Dynamics Code FUN3D - NASA/TM-2012-217771. Sponsoring Organization: NASA Langley Research Center.
- Bekemeyer, P., Ripepi, M., Götz, S., 2019. Nonlinear unsteady reduced-order modeling for gust-load predictions. *Amer. Inst. Aeronaut. Astronaut. AIAA J.* 57 (5), 1839–1850.
- Bisplinghoff, R.L., Ashley, R.L., Halfman, H., 1996. *Aeroelasticity*, 1996 ed. Dover, Constable, New York : London: New York, London.
- Cheung, R.C.M., Rezgui, D., Wilson, T., 2018. Testing of a hinged wingtip device for gust loads alleviation. *J. Aircr.* 55 (5), 2050–2067.
- Cook, M.V., Buonanno, A., Erbslöh, S.D., 2008. A circulation control actuator for flapless flight control. *Aeronaut. J.* 112 (1134), 483–489.
- Corporation, M.S., 2002. Msc. Nastran aeroelastic analysis user's guide. Printed in U.S.A.
- Edwards, J.W., Bennett, R.M., Seidel, D.A., 1983. Time-marching transonic flutter solutions including angle-of-attack effects. *J. Aircr.* 20 (11), 899–906.

- Forster, M., Steijl, R., 2015. Numerical simulation of transonic circulation control. In: 53rd AIAA Aerospace Sciences Meeting, AIAA 2015-1709.
- Forster, M., Steijl, R., 2017. Design study of coanda devices for transonic circulation control. *Aeronaut. J.* 121 (1243), 1368–1391.
- Frederick, M., Kerrigan, E.C., Graham, J.M.R., 2010. Gust alleviation using rapidly deployed trailing-edge flaps. *J. Wind Eng. Ind. Aerodyn.* 98 (12), 712–723.
- Guo, S., Los, J., Liu, Y., 2015. Gust alleviation of a large aircraft with a passive twist wingtip. *Aerospace* 2 (2), 135–154.
- Hoholis, G., Steijl, R., Badcock, K., 2016. Circulation control as a roll effector for unmanned combat aerial vehicles. *J. Aircr.* 53 (6), 1875–1889.
- Howcroft, C., Calderon, D., Lambert, L., Castellani, M., Cooper, J.E., Lowenberg, M.H., Neild, S., 2016. Aeroelastic modelling of highly flexible wings. In: 15th Dynamics Specialists Conference. American Institute of Aeronautics and Astronautics.
- Huvelin, F., Dequand, S., Liauzun, C., 2019. On the validation and use of high-fidelity numerical simulations for gust response analysis. *AerospaceLab* J. 1–16, ONERA.
- Jones, R.T., 1940. The Unsteady Lift of a Wing of Finite Aspect Ratio. NACA-TR-681.
- Levy, Y., 2001. Numerical simulation of dynamically deforming aircraft configurations using overset grids. *J. Aircr.* 38 (2), 349–354.
- Li, Y., Qin, N., 2019. Airfoil gust load alleviation by circulation control. *Aerosp. Sci. Technol.* 105622.
- Liu, X., Sun, Q., 2017. Improved LQG method for active gust load alleviation. *J. Aerosp. Eng.* 30 (4).
- Liu, J., Zhang, W., Liu, X., He, Q., Qin, Y., 2018. Gust response stabilization for rigid aircraft with multi-control-effectors based on a novel integrated control scheme. *Aerosp. Sci. Technol.* 79, 625–635.
- Min, B.-Y., Lee, W., Englar, R., Sankar, L.N., 2009. Numerical investigation of circulation control airfoils. *J. Aircr.* 46 (4), 1403–1410.
- Neumann, J., Mai, H., 2013. Gust response: Simulation of an aeroelastic experiment by a fluid–structure interaction method. *J. Fluids Struct.* 38, 290–302.
- Ng, B., Palacios, R., Kerrigan, E.C., Graham, J., Hesse, H., 2016. Aerodynamic load control in horizontal axis wind turbines with combined aeroelastic tailoring and trailing-edge flaps. *Wind Energy* 19 (2), 243–263.
- ohnston, J.F., 1979. Accelerated Development and Flight Evaluation of Active Controls Concepts for Subsonic Transport Aircraft. Volume 1: Load Alleviation/Extended Span Development and Flight Tests. (NASA-CR-159097).
- Parameswaran, V., Baeder, J.D., 1997. Indicial aerodynamics in compressible flow-direct computational fluid dynamic calculations. *J. Aircr.* 34 (1), 131–133.
- Paterson, E., Baker, W., Peltier, L., 2004. Rans and detached-eddy simulation of the NCCR airfoil. pp. 112–122.
- Payne, B.W., 1986. Designing a load alleviation system for a modern civil aircraft. In: (15th Congress of the International Council of the Aeronautical Sciences, ICAS-86-5.2.3).
- Raveh, D.E., Zaide, A., 2006. Numerical simulation and reduced-order modeling of airfoil gust response. *AIAA J.* 44 (8), 1826–1834.
- Rigaldo, A., Borglund, D., 2011. Aerodynamics Gust Response Prediction (Master's Thesis). Royal Institute of Technology.
- Rodden, W.P., Harder, R.L., Bellinger, E.D., 1979. Aeroelastic Additions to NASTRAN. Technical Report Contractor Report 3094, NASA.
- Rumsey, C.L., Nishino, T., 2011. Numerical study comparing RANS and LES approaches on a circulation control airfoil. *Int. J. Heat Fluid Flow* 32 (5), 847–864.
- Sclafani, A.J., Dehaan, M.A., Vassberg, J.C., Rumsey, C.L., Pulliam, T.H., 2014. Drag prediction for the common research model using CFL3D and OVERFLOW. *J. Aircr.* 51 (4), 1101–1117.
- Singh, R., Baeder, J.D., 1997. Direct calculation of three-dimensional indicial lift response using computational fluid dynamics. *J. Aircr.* 34 (4), 465–471.
- Song, Y., Li, Y., Chen, F., 2011. Two-dimensional simulation of circulation control turbine cascade. *Proc. Inst. Mech. Eng. G* 225 (7), 761–767.
- Szczyglowski, C.P., Neild, S.A., Titurus, B., Jiang, J.Z., Coetzee, E., 2019. Passive gust loads alleviation in a truss-braced wing using an inerter-based device. *J. Aircr.* 56 (6), 2260–2271.
- Timme, S., K.J., Badcock, Da Ronch, A., 2013. Linear reduced order modelling for gust response analysis using the DLR-tau code.
- de Vries, H., Boeije, C., Cleine, I., van Emden, E., Zwart, G., Stobbe, H., Hirschberg, A., Hoeijmakers, H., 2009. Fluidic load control for wind turbine blades. In: 47th AIAA Aerospace Sciences Meeting Including the New Horizons Forum and Aerospace Exposition. AIAA, pp. 2009–2684.
- Wetzel, D.A., Griffin, J., Cattafesta III, L.N., 2013. Experiments on an elliptic circulation control aerofoil. *J. Fluid Mech.* 730, 99–144.
- Wilde, P.I.A., Crowther, W.J., Harley, C.D., 2010. Application of circulation control for three-axis control of a tailless flight vehicle. *Proc. Inst. Mech. Eng. G* 224 (4), 373–386.
- Wright, J.R., 2015. In: Cooper, J.E. (Ed.), *Introduction to Aircraft Aeroelasticity and Dynamic Loads*, second ed. Wiley, Chichester, West Sussex, United Kingdom, 2015.